Calibrating the measurement of wavelength-dependent second harmonic generation from biological tissues with a BaB$_2$O$_4$ crystal

Mengzhe Shen
Jianhua Zhao
Haishan Zeng
Shuo Tang

SPIE

Calibrating the measurement of wavelength-dependent second harmonic generation from biological tissues with a BaB$_2$O$_4$ crystal

Mengzhe Shen,[a] **Jianhua Zhao,**[b] **Haishan Zeng,**[b] **and Shuo Tang**[a]
[a]University of British Columbia, Department of Electrical and Computer Engineering, Vancouver, BC, Canada
[b]British Columbia Cancer Agency Research Centre, Imaging Unit—Integrative Oncology Department, Vancouver, BC, Canada

Abstract. Although second harmonic generation (SHG) imaging has emerged as a powerful tool for imaging biological tissues with submicron resolution, the excitation wavelength dependence of SHG intensity in biological tissues is an optical property that is not fully understood so far. We first calibrate system factors which may potentially affect the accuracy of the wavelength-dependent SHG measurement. Then our calibration is validated by measuring the wavelength dependence of SHG signal from a BaB$_2$O$_4$ crystal under different focusing conditions and comparing with the theoretical calculations. The good agreement between the experimental results and theoretical calculations demonstrates that we have established a reliable method to validate wavelength-dependent SHG measurement over a broad wavelength range. We also investigate the wavelength dependence of a 10-μm thick mouse tendon tissue in both forward and backward directions. It is found that SHG of mouse tendon tissue decreases monotonically for excitation from 750 to 950 nm. © *2013 Society of Photo-Optical Instrumentation Engineers (SPIE)* [DOI: 10.1117/1.JBO.18.3.031109]

1 Introduction

Second harmonic generation (SHG) imaging has emerged as a powerful tool for imaging biological tissues with sub-micron resolution.[1–3] Two lower energy photons are up-converted to a higher energy photon with exactly twice of the incident photon frequency in a SHG process. Since the first practical SHG imaging on fiber bundle inside rat tail tendon in 1986, imaging collagen fibers in a variety of connective tissues and acto-myosin complexes in muscle have constituted the majority of applications of SHG. Besides qualitative visualization, a lot of efforts in the past decades have shown the promise of SHG in characterizing tissue optical properties quantitatively, such as the nonlinear $\chi^{(2)}$ matrix through polarization-dependent SHG imaging of endogenous myosin-rich muscle and collagen-rich tissues.[4–6]

The wavelength dependence of SHG intensity from collagen-rich tissue is an optical property that is not yet fully understood. Several publications presented different experimental results so far.[7–11] In Ref. 7, for collagen type I and III gel and rat tail tendon, with the excitation wavelength increasing from 740 to 960 nm, the SHG intensity was found to decrease monotonically by as much as one fifth. In Ref. 8, experimental studies on an organotypic RAFT tissue model (containing collagen) indicated that the SHG intensity had an oscillation pattern with maximum at 800 nm excitation. In Ref. 9, the authors observed a similar oscillation pattern that peaked at 840 nm excitation for mouse skin. Reference 10 showed four maxima of comparable intensities at 845, 880, 895, and 915 nm from a rat tendon cryosection and a bovine Achilles tendon measured in a backscattered geometry. Recently, more tissue types and tissue engineering scaffolds were measured in Ref. 11. It was found that polymer scaffold SHG peaked around 840-nm excitation, while bovine tendon collagen SHG tended to increase monotonically from 740 to 1000 nm. The authors also reported the effect of fixation on bovine tendon shifted the SHG excitation peak from 1000 to 840 nm.

From the above references, there are conflicting and controversial results on the wavelength-dependent SHG obtained by different research groups and among different tissue types. Part of the inconsistency could be due to the lack of a standard calibration and validation method. SHG depends on various factors such as the pulse width and polarization of the incident beam. For example, the SHG signal is inversely dependent on the pulse width. In addition, the way the dipole lies along the symmetry axis of the collagen may suggest how the SHG signal depends on laser polarization. Therefore, a calibration of these parameters is essential for a fair comparison among multiple wavelengths. On the collection side, transmission of the collection system and detector response can also vary over a broad wavelength range. In the above references, transmission/detector response calibration was executed either by a standard calibration lamp[8] or by standard fluorophores such as tryptophan in water and quinine sulfate in perchloric acid,[9] but the calibration methods were not described in detail. In many of the other above references, calibration methods were not mentioned. Therefore, a detailed investigation about the calibration method is necessary for investigating wavelength-dependent

Address all correspondence to: Shuo Tang, University of British Columbia, Department of Electrical and Computer Engineering, Vancouver, BC, Canada. Tel: 604-827-4314; Fax: 604-822-5949; Email: tang@ece.ubc.ca

SHG in biological tissues. In addition, there has been no report on a standard sample that can be used to validate the accuracy of the calibration methods.

In this paper, we will discuss the key factors affecting wavelength-dependent SHG. Details about how to verify those effects and perform system calibrations will be described. Furthermore, we propose to perform validation by measuring the wavelength dependence of SHG from a standard BaB_2O_4 (BBO) crystal and comparing it with theoretical calculations. For plane wave incidence, SHG intensity drops quickly when the excitation wavelength deviates from the designated phase-matching wavelength as determined by the angle cut of the BBO crystal. However, in the tight focusing condition, a strong SHG intensity can be excited over a broader range of excitation wavelengths because the focal length (approximately 1 to 2 μm) is even shorter than the coherence length of the SHG process (approximately 10 μm). Hence, we can utilize this effect to obtain a strong SHG over a wide wavelength range, and further use it as a standard to examine the accuracy of wavelength-dependent SHG measurement in tissues because the results from BBO can be predicted by theory. Other than the verification purpose, another aspect of investigating the SHG from BBO crystal is it is relatively easy to understand what factors affect its SHG wavelength dependence from the nonlinear coupled equation describing it, which further helps us understand the wavelength dependence in biological tissues.

This paper is organized as follows. First, we present the theoretical analysis of SHG from BBO crystal, emphasizing the factors affecting wavelength dependence of SHG. We follow this with a discussion about how to calibrate those system factors in experiment. Next, we show the wavelength-dependent SHG from BBO in an experiment with a collimated beam and focused beam for validation demonstration. Lastly, we measure the wavelength dependence of SHG from a thin sample of mouse tail tendon collagen and compare it with a preliminary theoretical calculation based on assumption about phase matching.

2 Materials and Methods

Due to the dispersion of BBO, it is not possible to achieve phase matching unless its birefringence property is utilized. BBO has two independent refractive indices $n_o(\lambda)$ and $n_e(\lambda)$, which are termed as the ordinary and extraordinary refractive index, respectively. The electrical field $E(\lambda)$ that propagates according to $n_o(\lambda)$ is orthogonal to the optic axis. Otherwise, it follows $n_e(\theta, \lambda)$, which is a function of the angle between the incident beam and the optic axis:[12]

$$n_o(\lambda)^2 = 2.7359 + \frac{0.01878}{\lambda^2 - 0.01822} - 0.01354\lambda^2 \quad (1)$$

$$n_e(\lambda)^2 = 2.3753 + \frac{0.01224}{\lambda^2 - 0.01667} - 0.01516\lambda^2 \quad (2)$$

$$\frac{1}{n_e^2(\theta, \lambda)} = \frac{\cos^2\theta}{n_o(\lambda)^2} + \frac{\sin^2\theta}{n_e(\lambda)^2}. \quad (3)$$

By adjusting the angle θ, the phase-matching condition $\Delta k = 2\pi[n_o(\lambda) - n_e(\theta, \lambda/2)]/\lambda = 0$ can be satisfied for a certain excitation wavelength. Only when Δk is zero, the energy from the fundamental wave can be efficiently transferred to the SHG wave. For the BBO used in this experiment, the angle between surface normal and optic axis is 29.3 deg, which helps achieve
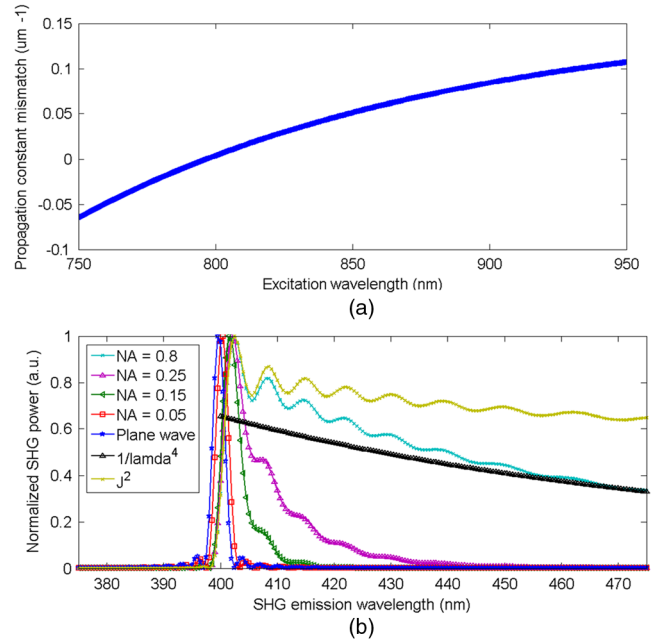
Fig. 1 (a) Calculated wavelength-dependent phase matching in BaB_2O_4 (BBO) crystal; (b) comparison of calculated wavelength-dependent second harmonic generation (SHG) power in different numerical aperture (NA) situations

phase matching for an excitation wavelength at 800 nm. In Fig. 1(a), we plot how Δk varies with excitation wavelength. When excitation wavelength is shorter than 800 nm, Δk is negative; while Δk is positive when the excitation wavelength is longer than 800 nm. It is also worth mentioning that the effective nonlinear coefficient d_{eff} depends on the projection of $E(\lambda)$ on each axis of the $\chi^{(2)}$ nonlinear susceptibility. Therefore, SHG generation efficiency is also related to the polarization of $E(\lambda)$.

Now, we try to deduce how the SHG power varies with excitation wavelength theoretically for both a collimated beam and focused Gaussian beam. For the sake of theory and experiment comparison, we will keep quantifying SHG strength by power within the whole text. For collimated wave incidence, it is assumed that we can apply the theory based on plane wave excitation because of its very low NA. The theoretical expression for SHG intensity, I_2, for plane wave excitation is given according to Ref. 13:

$$I_2 = \frac{8(\chi^{(2)})^2 \omega_2^2 I_1^2}{n_1^2 n_2 \varepsilon_0 c^3} L^2 \sin c^2 \left(\frac{\Delta k L}{2}\right), \quad (4)$$

where $\chi^{(2)}$, n_1, n_2, and ε_0 are the second order susceptibility, refractive index of excitation fundamental wave, refractive index of second harmonic wave, and vacuum permittivity, respectively. ω_2 is the frequency of SHG, and c is the speed of light. I_1 is the intensity of fundamental wave, L represents the thickness of the crystal, and Δk is phase mismatching. Equation (4) can be converted to the expression of power by using

$$P = \int I 2\pi r \mathrm{d}r, \quad (5)$$

where r represents the transverse distance from center. For a Gaussian beam with finite beam spot as $2\omega_0$, the power of SHG is given by

$$P_2 = \frac{1}{2}\pi\omega_0^2 I_2. \qquad (6)$$

The beam waist is given by

$$\omega_0 = \frac{1.27 \times f \times \lambda}{d} \approx \frac{1.27 \times \lambda}{2\text{NA}}, \qquad (7)$$

where d, f, and NA are the clear aperture, focal length, and numerical aperture of the lens, respectively. We are interested in wavelength-dependent SHG power when the fundamental power is kept constant. Substituting Eq. (4) into Eq. (6), while neglecting the terms that are not or less wavelength-dependent (such as n_2, n_1, and $\chi^{(2)}$), we have

$$P_2 = 16\left(\frac{2\pi}{\lambda_2}\right)^2 \frac{n_2(\chi^{(2)})^2 P_1^2}{\pi n_1^2 \varepsilon_0 c} \frac{\omega_{02}^2}{\omega_{01}^4} L^2 \sin c^2\left(\frac{\Delta k L}{2}\right)$$

$$\propto \frac{\sin c^2\left(\frac{\Delta k L}{2}\right)}{\lambda_2^2 \times \lambda_2^2}. \qquad (8)$$

Here ω_{01} and ω_{02} is the beam waist for the fundamental and SHG wave, respectively. The denominator of the right most expression in Eq. (8) consists of a product of two λ_2^2 terms. The first λ_2^2 term originates from time derivative term in the coupled wave equation, which indicates that higher frequency oscillation of the SHG dipole will generate a stronger, nonlinear effect. The other λ_2^2 term is due to the variation of beam diameter with wavelength. If we maintain the fundamental power as a constant, an increase of the beam waist will result in a decrease of peak intensity because SHG depends quadratically on the peak intensity.

In the tight focusing condition, which reflects the case when a high NA objective lens is used to focus light into the crystal, we first have the expression for the amplitude of SHG as Ref. 13,

$$A_2 = \frac{i\omega_2}{2n_2 c}\chi^{(2)}A_1^2 J_2, \qquad (9)$$

where A_1 and A_2 are complex amplitudes of the fundamental excitation and second harmonic wave, respectively, and J_2 is an integral from crystal surface z_0 to a certain depth z.

$$J_2(\Delta k, z_0, z) = \int_{z_0}^{z} \frac{e^{i\Delta k z'}dz'}{1 + 2iz'/b}. \qquad (10)$$

The confocal parameter b is defined as $b = k\omega_0^2$. By relating amplitude with intensity, we have

$$I = 2n\varepsilon_0 c|A|^2, \qquad (11)$$

and using Eqs. (6) and (7), we have

$$P_2 = \frac{1}{4}\left(\frac{2\pi}{\lambda_2}\right)^2 \frac{n_2(\chi^{(2)})^2 P_1^2}{\pi n_1^2 \varepsilon_0 c}\frac{\omega_{02}^2}{\omega_{01}^4}J_2^2 \propto \frac{1}{\lambda_2^4}J_2^2. \qquad (12)$$

From the above derivation, we can see that the wavelength dependence of SHG power depends on not only phase matching but also variation of beam waist for both a collimated and focused wave.

Figure 1(b) shows the SHG power versus wavelength for different NAs of focusing lens. The dispersion property of the crystal is calculated from Eqs. (1)–(3). The SHG power for different NAs are normalized and compared with collimated beam in Fig. 1(b). For the collimated beam, since the phase mismatch Δk is critical for a strong SHG emission, the pattern follows a sinc-squared function that peaks at 400 nm. When the NA is as small as 0.05, its pattern is very similar to that of a plane wave, except for a peak wavelength shift which will be explained later. It validates our treatment of collimated beam as plane wave. For NA = 0.15 and 0.25, after a steep rise and peak around 400 nm, the emission SHG power decreases slower than in the plane wave case when the excitation wavelength deviates from the phase matching excitation wavelength. One may notice that the peak wavelength in this case is shifted from 400 nm to a longer wavelength compared with the plane wave and NA = 0.05 cases. This is because the fundamental wave experiences a Gouy π phase shift in the focal region within a length equal to the confocal parameter of the beam, which reduces the effective propagation constant k in the focal volume.[14] Therefore, only if there exists a positive phase mismatch (for crystal we use, it is generated by excitation wavelength longer than 800 nm) can we achieve perfect phase matching in the focal volume. Otherwise, at the wavelength region where originally we have Δk equal to or smaller than a zero phase mismatch, the phase matching condition deteriorates such that the SHG power is greatly reduced. This explains the fast decreasing of SHG power when the excitation wavelength is shorter than the peak wavelength. It is also observed that a uniformly spaced oscillation structure is superposed on the decaying pattern, which originates from the relative phase of a particular excitation wavelength compared with that of the peak wavelength.[15] When the NA is even higher, the SHG power reduces slower with wavelength change than lower NA cases. For example, with NA = 0.8, the SHG power reduces to around 40% when the excitation wavelength varies from 800 to 950 nm. In order to distinguish the contribution of J_2^2 and $1/\lambda^4$ in Eq. (12) to the pattern of NA = 0.8 curve, the wavelength dependence of these two terms are plotted separately. When the excitation wavelength is close to optimum phase matching (corresponding to a better phase mismatch), the wavelength dependence is dominated by J_2^2; when the excitation wavelength deviates from optimum phase matching wavelength (corresponding to a worse phase mismatch), the tail of the oscillating decreasing curve approaches the $1/\lambda^4$ term. These observations will be helpful when we investigate the wavelength dependence of SHG from collagen in later sections.

Figure 2 is a schematic drawing of the optical layout of the measurement system setup. The light source is a mode-lock titanium-sapphire laser (Chameleon, Coherent, USA) providing wavelength tunable femto-second laser pulse from 720 to 960 nm. A combined half wave plate ($\lambda/2$, 10RP52-2 Newport) and polarization beam splitter (PBS, PBS052 AR600-1000 nm, Thorlabs, USA) module is used for coarse control of the excitation laser power. The fine control of the laser excitation power at different wavelengths is achieved by rotating a variable neutral density (ND) filter wheel (NDC-50C-2M-B, Thorlabs, USA). In order to retain the polarization state of excitation light at all wavelengths, a dichroic glass polarizer (POL 1, VISIR 600 to 1200 nm, color Pol, USA) is used. The laser beam is expanded by two lenses (L1, L2) with focal lengths of 25 and 250 mm, respectively, so that the back aperture of
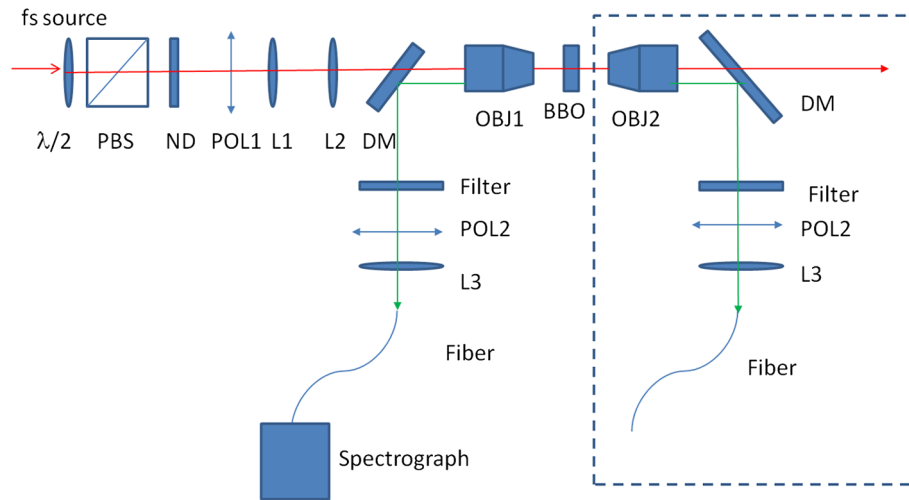
Fig. 2 Experimental setup for wavelength-dependent second harmonic generation (SHG) measurements in forward and backward directions from BaB_2O_4 (BBO) and tendon tissue

the objective lens is filled, after which the laser beam is cast onto the sample by a 40× (NA = 0.8) objective (OBJ1, LUMPLFLN, Olympus, USA). For comparison purposes, the 40× objective lens can be replaced with a 10× (NA = 0.25) objective (Plan N, Olympus, USA) or completely removed away for collimated beam excitation. The backward SHG is collected by the same objective and directed to a spectrograph through a long pass dichroic beam splitter (DM, FF660-Di02, Semrock, USA). The residual excitation fundamental wave is further attenuated by a band-pass filter (FF01-750, Semrock, USA). Another polarizer (POL2) (LPVISE100-A, Thorlabs, USA) is placed before the focusing lens (L3) to examine the polarization state of the SHG signal. The focusing lens has a focal length of 75 mm. The 1-m long multimode fiber (FG200-UCC, Thorlabs, USA) used has a 200-μm core diameter with NA = 0.22. Spectral measurements are obtained with a spectrograph with a resolution of 0.5 nm (SpectraPro-150, Roper Scientific, USA), which is directly coupled to the multimode fiber. The dashed part in Fig. 2 is a setup for collecting forward SHG signal which includes a 60× (NA = 1.0) objective (LUMPLFLN, Olympus, USA). The remaining components are exactly the same as what are used in the backward path.

Besides the factors such as phase mismatching and intensity variation, we try to calibrate system factors that may affect the measurements of the wavelength-dependent SHG. In the following, we will discuss this issue in the context of using 40× objective lens because it is directly related to our calibration purpose. These factors can be examined in the order of how the SHG signal is generated and collected with four steps.

First, properties of the excitation beam that affect the SHG power should be kept constant for each wavelength. For example, the excitation power under different excitation wavelengths is controlled by rotating the angle of the variable ND filter wheel. The angle of the filter is calibrated for each wavelength so that the excitation power, monitored by a wavelength calibrated silicon-based power meter (S132A 600-1000 nm, Thorlabs, USA), is kept the same after the objective. An autocorrelator (FR 103M, Femtochrome Research, USA) is used to measure the laser pulse width before the objective, and pulse width variation is not significant as shown in Fig. 3(a) assuming a hyperbolic secant pulse shape. As we mentioned earlier, the

polarization of the excitation beam must be kept the same for all the wavelengths because the effective nonlinear coefficient depends on polarization. By rotating the angle of polarizer POL1 then measuring the laser power at different angles and four excitation wavelengths separated by 50 nm [shown in Fig. 3(b)], we find that the polarization state of excitation laser before objective is the same for all the wavelengths. If we compare the angle-dependent power with a cosine square function, which represents a linear polarization, the incident light is confirmed to be linearly polarized.

Then we need to make sure that all these factors are not altered at the focal spot inside the BBO crystal. The transmission curve of BBO in the 700- to 1000-nm range is quite flat. Therefore, we can reasonably assume the excitation power is the same for all the wavelengths over the laser tuning range at the focal point.[16] The effect of group velocity dispersion from the crystal and objective lens on the pulse-width broadening can be calculated by

$$t = \tau_0 \sqrt{1 + \left(\frac{4 \ln 2 D}{\tau_0^2}\right)^2}, \qquad (13)$$

where t is the broadened pulse width, τ_0 is the original pulse width, and D is the group velocity dispersion. It is estimated that for a 1-mm thick BBO crystal and a 40× objective lens, D is roughly 200 and 6500 fs^2, respectively.[17] Even for a large dispersion, such as 6500 fs^2, the pulse will be broadened by only 10% for a 170-fs pulse width, which indicates that the pulse-broadening effect is not significant for the pulse width we use. Hence, pulse widths for different wavelengths are considered to be the same at the focal point. High NA objectives can affect the polarization state of the excitation beam due to either the anti-reflection coating of the lens or the angle of incidence beam. The polarization state of the excitation beam at the focal point can be examined by analyzing the polarization state of the SHG signal. The polarization state of the excitation beam at the focal point can be examined by analyzing the polarization state of the SHG signal because the polarization state of the excitation light (o light) and emission light (e light) are orthogonal with each other. Therefore, if the polarization state of the SHG signal is the same for all the wavelengths, the corresponding
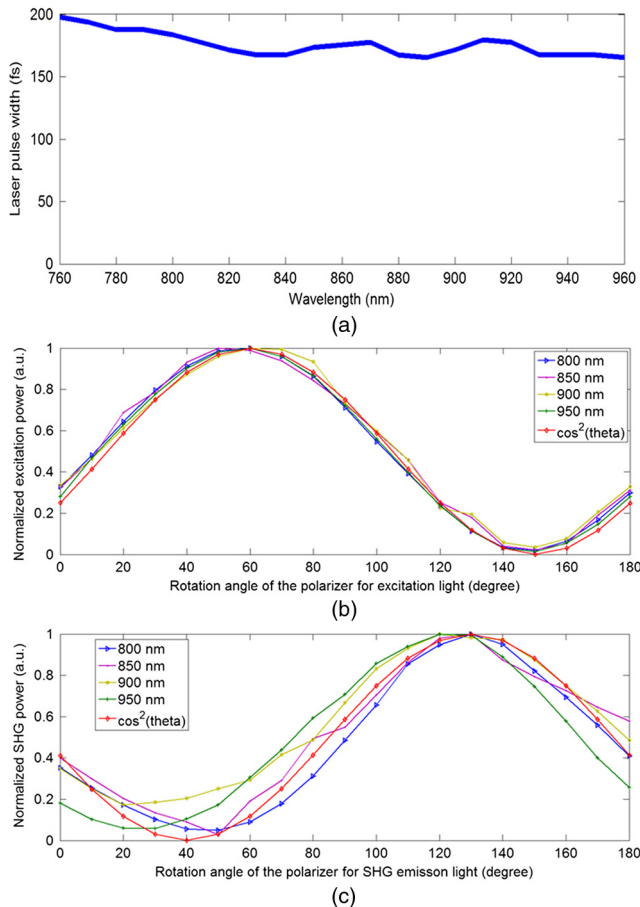
Fig. 3 (a) Pulse width measurement results before objective lens; (b) plot of excitation power versus analyzer angle at different wavelengths; (c) plot of emission power versus analyzer angle at different wavelengths

excitation fundamental wave must have the same polarization state as well. Figure 3(c) shows the polarization state of the SHG signal by rotating POL2 at excitation wavelengths ranging from 800 to 950 nm, at a 50-nm step. We find they all fit with linear polarization and the peaks are located at the same rotation angle, indicating that polarization of the excitation and emission beams at the focal point are the same for different excitation wavelengths.

After the SHG signal is generated at the focal point, we must make sure they are collected equally at different wavelengths. The profile of the excitation fundamental beam at the focal point is Gaussian, which is described by the confocal parameter b and beam radius ω_0. For the SHG wave, b matches the excitation wave, but the SHG's beam waist is smaller than the excitation wave because SHG has a larger propagation constant k. Hence, the divergence angle of the SHG wave given by arctan (b/ω_0) will be smaller than that of the fundamental wave. It ensures that for either forward or backward transmitted SHG, it will be collected by the objective lenses with the same NAs. When the excitation wavelength changes, the confocal parameter b and beam radius ω_0 both change accordingly; however, the angular divergence of the beam, given by $\theta = \lambda/\pi\omega_0$, is the same for all the wavelengths.[13] Therefore, we expect the collection conditions for SHG at different wavelengths are the same. In the case of SHG from BBO crystal, backward collected SHG comes from the reflection of forward SHG at the interface of crystal and air. When the focal point approaches the interface, more SHG signal will be collected by the objective. The focal point in the crystal may vary at different wavelengths due to achromatic aberration, but considering the scale of the variation and the uniformity of the crystal, it is considered insignificant in our experiment.

Finally, to fairly compare the SHG signal on the spectrometer at different wavelengths, transmission/detector response calibration for the detection system at different wavelengths is also necessary. One method to apply the transmission/detector response calibration is to divide the factory-supplied, National Institute of Standard and Technology (NIST) traceable spectrum of a standard intensity calibration lamp by the measured spectrum from the system so that the transmission/detector response correction coefficient of the system is obtained. In order to guide the light from the lamp uniformly to the objective lens, a two-port integrating sphere is used, in which one port collects the lamp light while the other port transmits the light into the objective. The integrating sphere functions as a diffuser so that light rays from standard calibration lamp are uniformly cast onto the front aperture from all the incident directions. In Fig. 4(a), the black curve represents the known output of the lamp, and the red curve represents the spectrum measured by the system. The resulting correction coefficient shown by the green curve can be used to compensate for the transmission/detector response at different wavelengths by multiplying it with the raw spectrum of any new measurements by the system. The accuracy of the calibration will dramatically affect the wavelength-dependent measurement. Therefore, we verified the correctness of our calibration by measuring one- and two-photon fluorescence emission spectrum of an NADH (nicotinamide adenine dinucleotide) sample. It was previously found that one- and two-photon fluorescence properties of NADH are the same.[18] Hence, by comparing the one- and two-photon emission spectra of NADH, the correctness of transmission calibration can be verified. The one-photon emission spectrum of NADH was measured using a separate spectrofluorometer equipped with two double-grating monochromator.[19] In Fig. 4(b), before calibration, the peak of the two-photon fluorescence emission is at 480 nm, and after calibration the peak is shifted to 450 nm. The overlap of the one- and two-photon emission spectra over the whole wavelength range indicates that our calibration method is correct. The results also demonstrate the importance of the transmission/detector response calibration.

3 Results and Discussions

Based on the above procedures for wavelength-dependent measurement, the calibrated wavelength-dependent SHG from a BBO crystal is measured and plotted in Fig. 5. The spectra are first recorded by the spectrometer then multiplied by the transmission/detector response correction coefficient. The emission spectra for the 40× objective, 10× objective, and collimated beam are plotted in Fig. 5(a)–5(c), respectively. Each emission spectrum is further integrated over its wavelength span to get the total SHG power and compared with theoretical calculations. In order to take into account the finite line width of the laser, the theoretically calculated SHG power are averaged over each 10-nm bandwidth based on the spectrum shape. This processing makes the curves less oscillating than those shown in Fig. 1(b). In Fig. 5(d), it is observed that the SHG collected in the backward direction in the three different cases all match well with the theory. For the 40× objective case, some amount of SHG signal

(a)

(b)
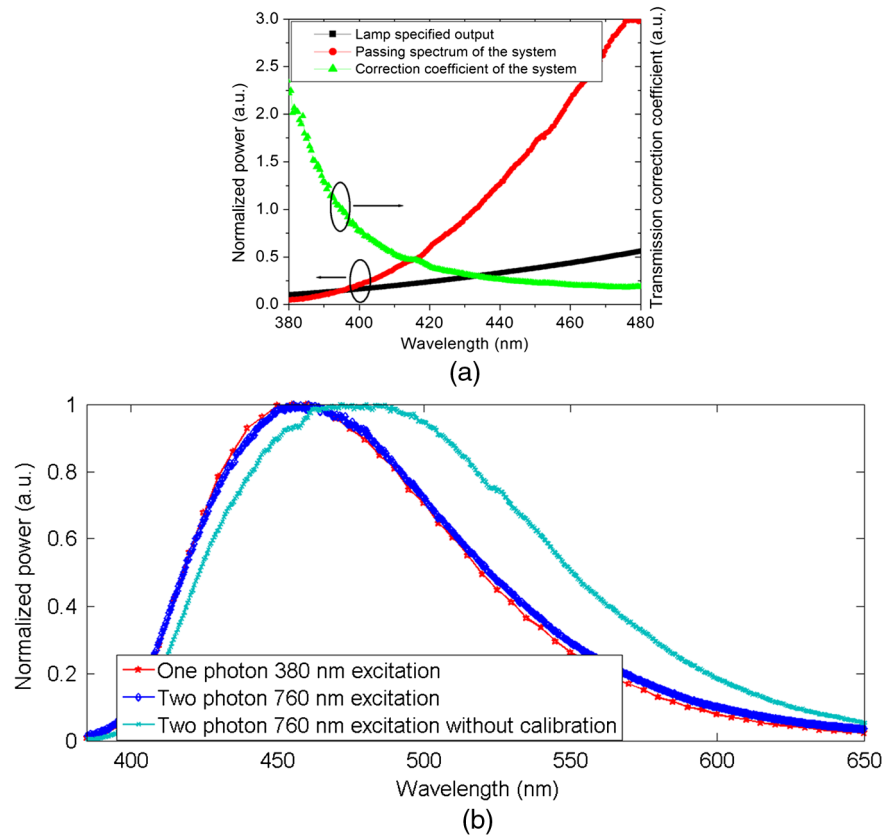
Fig. 4 (color online) (a) Factory-supplied NIST (National Institute of Standard and Technology) traceable spectrum of the standard lamp (black) and the lamp spectrum measured by our optical system (red) with which transmission/detector response correction coefficient is calculated (green); (b) one- and two-photon fluorescence emission spectrum for NADH with or without transmission/detector response calibration.
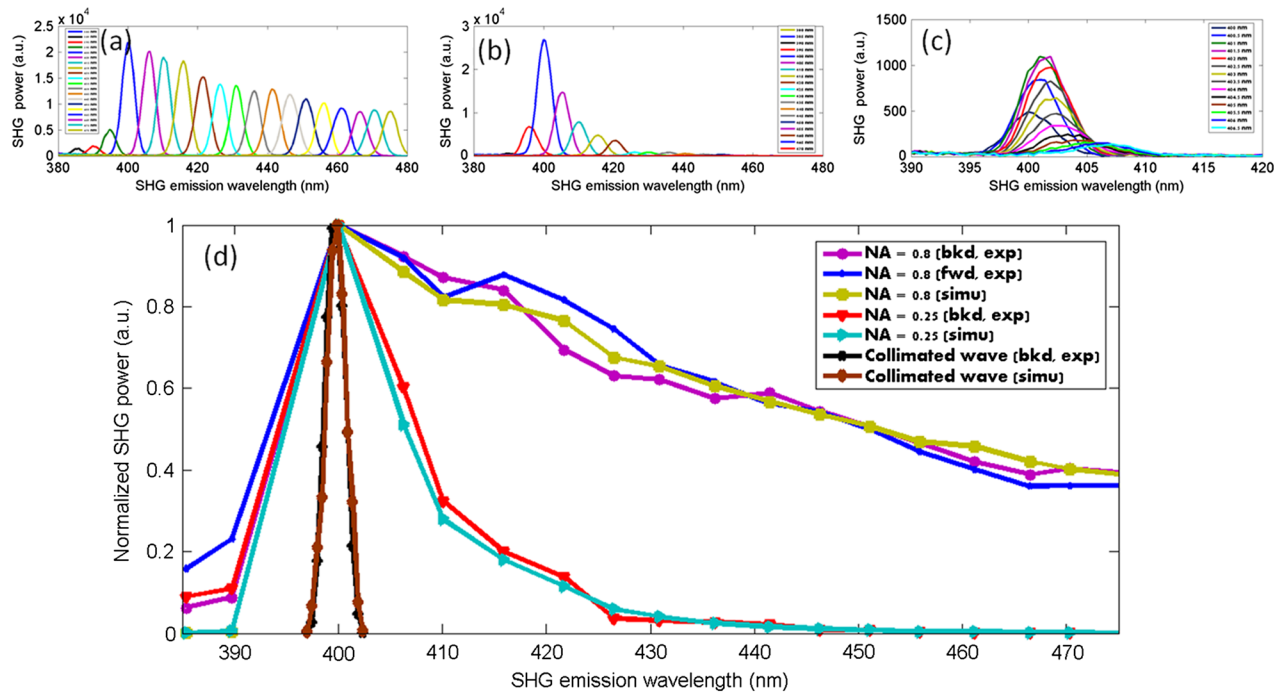
Fig. 5 Experiment results for wavelength-dependent second harmonic generation (SHG) power versus emission wavelength with (a) 40× objective (NA = 0.8), (b) 10× objective (NA = 0.25), and (c) collimated beam; (d) theoretical and experimental comparison for wavelength-dependent SHG power for collimated beam and focused beams.

is collected below 400 nm despite a prediction of null in theory. This is likely because the angle spread of propagation constant $k(\lambda)$ due to focusing makes it possible to achieve perfect phase matching at wavelengths shorter than 800 nm. It also happens with less-tight focusing, such as the 10× objective case, but it is absent from the plane wave case. The peak wavelength shifts for the collimated beam and focused beam are also less obvious in the experimental cases, which is largely due to the fact that the 10-nm laser bandwidth is broader than the peak wavelength shift. Also, the forward- and backward-collected SHG at NA = 0.8 have similar wavelength dependence trends, which matches with the fact that the source of backward-collected SHG is purely the reflection of forward SHG.

We also measured the wavelength-dependent SHG from a mouse tail tendon tissue with a 10-μm thickness cut from a tendon tissue by a cryostat microtome. Some wavelength-dependent features are similar for both the crystal and mouse tail tendon tissues, such as the two $1/\lambda^2$ terms originating from oscillation of dipoles and variation of focal volume that contributes to a total of $1/\lambda^4$ dependence for SHG from the crystal. There are also quite a few differences between the crystal and tissue SHG wavelength-dependence. Firstly, in spite of the fact that phase matching in the crystal is very clear, as long as the wavelength dependent refractive index and polarization state of the incident beam are known, the phase matching condition is not yet clear for the tendon. Secondly, the sources of collected SHG signal from tissue may include the scattered SHG signal, as collagen is a highly scattering medium. For collagen fibers, we found Mie scattering ascribed to the fibrils whose thickness is around a few micrometers, and Rayleigh scattering resulting from banded striation in fibrils at the ultra-structure level. These two scattering process have different wavelength dependencies, and Ref. 20 claims that a combination of Mie and Rayleigh scattering can explain some of the scattering coefficient measurement in skin. According to Ref. 8, the average mean free path in tissue due to scattering is on the order of 100 μm. Therefore, considering the thickness of the tendon tissue we measured, the scattering effect should not affect the results of the 10-μm thick tissue sample.

In Fig. 6, we plot the wavelength dependent SHG from mouse tail tendon in both forward and backward directions. Each data point is an average of six measurements. The insertion shows the polarization property of the received SHG signal. The SHG power is first maximized by rotating the polarization of the laser with a half wave plate (10RP12-28, Newport, USA).
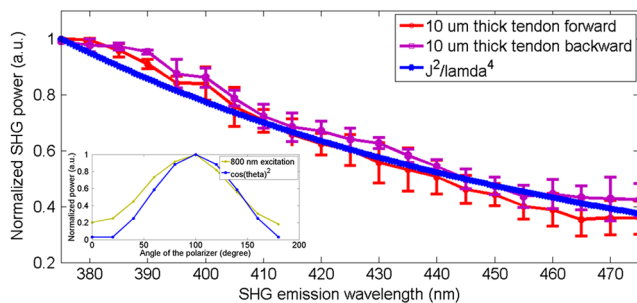
Fig. 6 Wavelength-dependent second harmonic generation (SHG) power from 10-μm mouse tail tendon for both forward and backward directions, and its comparison with J_2^2/λ^4 curve for $\Delta k = 0.4$ μm^{-1} and NA = 0.8. (Inset) dependence of SHG signal power on angle of polarizer POL2 for 800-nm excitation. The curves are compared with $\cos^2 \theta$ function.

Then the POL2 in the detection path is rotated, and the variation of the SHG power is measured and plotted. The plot shows that the SHG signal is close to linear polarization, and the nonzero values at 0 and 180 deg may be due to the fact that the polarizer is nonideal and the laser has a bandwidth. Our experimental results show that when the excitation wavelength increases, both the forward and backward SHG power decreases monotonically. From short to long wavelengths, the power decreases approximately by 60%. Qualitatively, our results are similar to Ref. 7, but different from the rest studies.[8–11] It is also observed that the normalized wavelength-dependent trends for forward and backward SHG are not significantly different except that the forward power is slightly stronger than the backward power.

There are two possible sources for the backward-collected SHG from thin tissue: (1) the backward SHG may be the reflection of forward SHG at the tissue-air interface. Hence, the wavelength dependence should not be altered; (2) the backward-collected SHG may originate from the generation of SHG in the backward direction, and how it may affect the wavelength dependence of SHG depends on the mechanism of phase matching in the backward direction. Backward SHG may be generated in tissue due to quasi-phase matching.[21]

As the scattering effect is minimal in thin tissue, the wavelength-dependent collagen SHG may be explained by the expression J_2^2/λ^4. Since there is no proved wavelength-dependent refractive index expression for collagen, we assume Δk is constant over the full excitation wavelength span in the simulation. We calculated the normalized J_2^2/λ^4 over the full wavelength range, and found that when $\Delta k = 0.4$ μm^{-1} the simulated result qualitatively fits with experimental result for the thin collagen sample. The slope of J_2^2/λ^4 depends on Δk, which can be interpreted more easily with the help of the analytical solution of J_2 in the limiting case where b is much smaller than the thickness of the material. In this limiting case, the analytical solution to Eq. (10) is given by

$$J_2 = \frac{b}{2}(2\pi)\exp\left(-b\Delta k/2\right). \tag{14}$$

For a given NA, the exponential term decreases when wavelength increases because the confocal parameter b is proportional to wavelength, but on the other hand, the $b/2$ term increases with the excitation wavelength. Therefore, how J_2 varies with excitation wavelength depends on the product of these two terms. The value of Δk will determine which term is dominant in determining the shape of the wavelength dependence, but it is not difficult to summarize that when Δk is larger, the decrease of J_2^2/λ^4 is sharper, taking into account the $1/\lambda^4$ term. In normal dispersion material, the phase mismatch between the excitation wave and SHG wave will decrease with increasing excitation wavelength. In that circumstance, the simulated curve may become steeper at shorter excitation wavelength while flatter at longer excitation wavelength.

4 Conclusions

In summary, the calibration procedures for wavelength-dependent SHG measurements are introduced. The accuracy of calibration procedures is proved by measuring the SHG wavelength dependence in a BBO crystal. The agreement between theory and experiment for the BBO crystal demonstrates that our proposed method can be used as a validation method when investigating the wavelength dependence of SHG from biological tissues. In the end, the wavelength dependence of

SHG from a mouse tail tendon tissue is measured for a 10-μm thick sample. It was observed that the SHG power decreases monotonically from 750 to 950 nm excitations.

Acknowledgments

References

1. I. Freund, M. Deutsch, and A. Sprecher, "Connective tissue polarity optical second-harmonic microscopy, crossed-beam summation, and small-angle scattering in rat-tail tendon," *Biophys. J.* **50**(4), 693–712 (1986).
2. P. J. Campagnola et al., "Three-dimensional high-resolution second-harmonic generation imaging of endogenous structural proteins in biological tissues," *Biophys. J.* **82**(1), 493–508 (2002).
3. P. J. Campagnola and L. M. Loew, "Second-harmonic imaging microscopy for visualizing biomolecular arrays in cells, tissues and organisms," *Nat. Bio.* **21**(11), 1356–1360 (2003).
4. S. Psilodimitrakopoulos et al., "*In vivo*, pixel resolution mapping of thick filaments' orientation in nonfibrilar muscle using polarization-sensitive second harmonic generation microscopy," *J. Biomed. Opt.* **14**(1), 014001 (2009).
5. S. V. Plotnikov et al., "Characterization of the myosin based source for second harmonic generation from muscle sarcomeres," *Biophys. J.* **90**(2), 693–703 (2006).
6. F. Tiaho, G. Recher, and D. Rouede, "Estimation of helical angles of myosin and collagen by second harmonic generation imaging microscopy," *Opt. Express* **15**(19), 12286–12295 (2007).
7. W. Zipfel et al., "Live tissue intrinsic emission microscopy using multi-photon-excited native fluorescence and second harmonic generation," *Proc. Natl. Acad. Sci. USA* **100**(12), 7075–7080 (2003).
8. A. Zoumi, A. Yeh, and B. J. Tromberg, "Imaging cells and extracellular matrix in vivo by using second harmonic generation and two-photon excited fluorescence," *Proc. Natl. Acad. Sci. USA* **99**(17), 11014–11019 (2002).
9. J. Palero et al., "Spectrally resolved multiphoton imaging of in vivo and excised mouse skin tissues," *Biophys. J.* **93**(3), 992–1007 (2007).
10. T. Theodossiou et al., "Second harmonic generation confocal microscopy of collagen type I from rat tendon cryosections," *Biophys. J.* **91**(12), 4665–4677 (2006).
11. H. J. Askew and S. J. Matcher, "Investigation of the wavelength dependence of SHG from various tissues," A. Periasamy, K. Konig, and P. T. C. So, Eds., *Proc. SPIE* **8226**, 82261G (2012).
12. K. Kato, "Second-harmonic generation to 2048A in B-Ba$_2$O$_4$," *J. Quantum Electron.* **22**(7), 1013–1014 (1986).
13. R. W. Boyd, *Nonlinear Optics*, Academic Press, Boston (2003).
14. J. Cheng, A. Volkmer, and X. S. Xie, "Theoretical and experimental characterization of coherence anti-Stokes Raman scattering microscopy," *J. Opt. Soc. Am. B.* **19**(6), 1363–1375 (2002).
15. G. D. Boyd and D. A. Kleinman, "Parametric interaction of focused Gaussian light beam," *J. Appl. Phys.* **39**(8), 3597–3639 (1968).
16. D. C. Edelstein, E. S. Wachman, and C. L. Tang, "Broadly tunable high repetition rate femtosecond optical parametric oscillator," *Appl. Phys. Lett.* **54**(18), 1728–1730 (1989).
17. J. B. Guild, C. Xu, and W. W. Webb, "Measurement of group delay dispersion of high numerical aperture objective lenses using two-photon excited fluorescence," *Appl. Opt.* **36**(1), 397–491 (1997).
18. S. Huang, A. A. Heikal, and W. W. Webb, "Two-photon fluorescence spectroscopy and microscopy of NAD(P)H and flavoprotein," *Biophys. J.* **82**(5), 2811–2825 (2002).
19. J. Zhao et al., "Assessing topographic cutaneous autofluorescence variation using fluorescence UV and visible excitation emission matrix (EEM) spectroscopy," N. Kollias, Ed., *Proc. SPIE* **7883**, 78830I (2011).
20. I. S. Saidi, S. L. Jacques, and F. K. Tittel, "Mie and Rayleigh modelling of visible-light scattering in neonatal skin," *Appl. Opt.* **34**(31), 7410–7418 (1995).
21. R. Lacomb et al., "Phase matching considerations in second harmonic generation from tissues: effects on emission directionality, conversion efficiency and observed morphology," *Opt. Commun.* **281**(7), 1823–1832 (2008).